Topology optimization for the computationally poor: efficient high resolution procedures using beam modeling

Eilam Amir Oded Amir

July 16, 2018

Abstract

A structural optimization approach based on beam modeling is formulated and investigated. Its computational efficiency and enhanced design freedom place it as a computationally cheap alternative to continuum topology optimization. The optimization uses a ground structure parametrization and consists of alternating shape and sizing-topology design phases. The sizing-topology phase controls the thicknesses of tapered beams. Linear constraints applied in the shape phase provide regularity and consistency to the structure and enable the shape design variables to benefit from large freedom of movement. A direct comparison to continuum-based topology optimization shows that the beam-based optimization can offer significant computational savings while generating designs that perform similarly to continuum designs. The result of the beam optimization can be utilized also as an effective starting point for further design iterations on a refined continuum model. The reduced computational effort facilitates the optimization of high resolution structures without separating to micro and macro scales, hence non-uniform and non-periodic porous structures can be designed in a single-level optimization process. Furthermore, the beam modeling allows to impose minimum and maximum length scales explicitly without any additional constraints. The applicability of the suggested approach is demonstrated on several cases of stiffness maximization and mechanism design.

1 Introduction

Over the last three decades since it was introduced by Bendsøe and Kikuchi [1988], continuum topology optimization has evolved and matured into a widely accepted computational design method. For comprehensive reviews of the various approaches and procedures, the reader is referred to recent review articles [Sigmund and Maute, 2013, Deaton and Grandhi, 2014]. Nowadays, the growing availability of computational resources together with the rise of Additive Manufacturing (AM) promote the utilization of high resolution continuum finite element models as the basis for topology optimization.

High resolution topology optimization is utilized primarily in the context of two different design goals: 1) Macro-level design of a single structural component; and 2) Micro-level design of a meta-material. For the first class of applications, Aage et al. [2014] introduced a parallel computing framework for CPUs. In the same spirit, adapting topology optimization procedures for parallel computing on GPUs has attracted considerable interest, and the reported computational times appear very promising [e.g. Wadbro and Berggren, 2009, Schmidt and Schulz, 2011, Suresh, 2013, Zegard and Paulino, 2013, Challis et al., 2014, Gavranovic et al., 2015, Wu et al., 2016b]. Typical finite element discretizations used for macro-level design consist of hundreds or thousands of elements in each spatial dimension, leading to models with up to hundreds of millions of finite elements, in extreme cases even billions [Aage et al., 2017]. The second class of applications that essentially relies on the inverse homogenization method [Sigmund, 1994, 2000], has also benefited from the availability of high performance parallel computing. Examples include the design of three-dimensional extremal elastic microstructures, based on either CPU [Andreassen et al., 2014] or GPU [Challis et al., 2014] parallel computing.

An even more challenging design goal combines both macro and micro levels in a single design space, based on the capability of AM to realize such structures. Bridging macro and micro scales is still very challenging from a computational perspective because it requires to model the full design domain (macro level) while allowing very small design features (micro to meso level). In recent years, several methods were suggested for bridging the scales. Free Material Optimization (FMO) on the macro scale was combined with inverse homogenization on the micro/meso scale [Schury, 2013, Schury et al., 2012]. Continuity was achieved by imposing constraints on both scales so that the optimization process leads to a varying porous layout which is then realized by AM. Alexandersen and Lazarov [2015] suggested a multilevel approach in which the full design domain is optimized without any length scale separation based on MsFEM (Multiscale Finite Element Method). However, MsFEM still requires domain partitioning for an eigenvalue problem formulation; its solution serves repeatedly as a preconditioner for solving the full system of equations. Hence, the outcome is a varying porous layout with certain periodic properties. Recently, Groen and Sigmund [2017] revisited the square cell parametrization that was used originally by Bendsøe and Kikuchi [1988] to derive the first topology optimization solutions. In the first stage, the density and rotation of each cell are optimized on the macro level based on homogenization and using a relatively coarse grid. In the second post-processing stage, these values are projected to the actual fine scale, leading to high-resolution layouts at a low computational cost.

In both macro- and micro-scale design it is noticeable that the outcome of continuum-based procedures often consists of beam-like members with various shapes and different sizes. This motivates the formulation of simplified procedures, based on beam modeling, that can reduce the computational cost significantly. This is the central aim of the current study. The suggested formulation is based on the well-known ground structure parametrization consisting of tapered beams with two alternating phases of shape and sizing-topology. The shape phase controls nodal movements and the sizing-topology controls the tapered beam nodal thicknesses.

The ground structure parametrization is not new and its utilization in coupled shape-topology procedures for trusses has been discussed in the literature [Ben-Tal et al., 1993, Achtziger, 2007]. The current study involves tapered beam modeling and presents several contributions in the context of topology optimization: (1) The ability to enhance the design freedom by imposing a set of linear constraints for the coordinated movement of nodes, while providing regularization to the optimized structures; (2) The ability of the suggested scheme to obtain high quality topological layouts with low computational cost, and its direct and fair comparison to continuum procedures; (3) The ability to suggest solutions for complex problems such as non-periodic high resolution designs and the explicit imposition of a maximum length scale; (4) The consistent and differentiable treatment of the singularity associated with tapered beam formulations, following a power series approximation [Cleghorn and Tabarrok, 1992].

The outline of the paper is as follows: In Section 2, the structural modeling of the tapered beam ground structure is explained, including a discussion on the singularity of the prismatic case and how it is resolved in a differentiable manner. Optimization based on the alternating shape and sizing-topology optimization process is presented in Section 3. Then, Section 4 describes an objective approach for comparison to continuum-based optimization procedures. Numerical examples are presented in Section 5, including both macro-level designs and high resolution fine scale designs without length scale separation. Finally, some conclusions, insights and implications are presented in Section 6.

2 Structural modeling

As the optimization procedure is based on a discrete ground structure parametrization, it is essential to gain enough design freedom so it can emulate effectively the continuum approach. One of the measures to achieve this goal is by using tapered beam members to construct the ground structure. The tapered beam formulation is hereby presented.

2.1 Tapered beam formulation

The beam stiffness is modeled using the Euler-Bernoulli assumption of zero shear deformation. Extending the formulation to consider also shear deformations is not a difficult task, yet it has been observed during numerical studies that shear deformations have little influence on the outcome of the optimization. Derivation of the stiffness matrix of the tapered beam follows the common flexibility method as described in Weaver and Gere [2012] and in similar textbooks; it is verified by comparing to Eisenberger [1991]. For a linearly tapered beam as presented in Figure 1, the stiffness matrix is given by

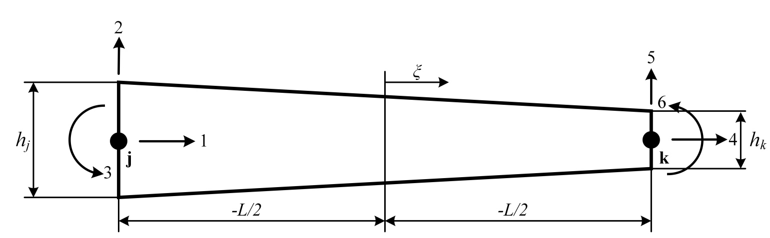

Figure 1: A parametrized linearly tapered beam

$$\mathbf{K}_m = \begin{bmatrix} s_{11,ex} & 0 & 0 & -s_{11,ex} & 0 & 0 \\ 0 & s_{22,ex} & s_{23,ex} & 0 & -s_{22,ex} & s_{26,ex} \\ 0 & s_{23,ex} & s_{33,ex} & 0 & -s_{23,ex} & s_{36,ex} \\ -s_{11,ex} & 0 & 0 & s_{11,ex} & 0 & 0 \\ 0 & -s_{22,ex} & -s_{23,ex} & 0 & s_{22,ex} & -s_{26,ex} \\ 0 & s_{26,ex} & s_{36,ex} & 0 & -s_{26,ex} & -s_{36,ex} + s_{26,ex}L \end{bmatrix} \tag{1}$$

with the following coefficients,

$$s_{11,ex} = \frac{Eb}{L}\left[\frac{c}{\ln\left(\frac{2\bar{h}+c}{2\bar{h}-c}\right)}\right] \tag{2}$$

$$s_{22,ex} = \frac{Eb}{12L^3}\left[\frac{c^3\bar{h}}{\bar{h}\ln\left(\frac{2\bar{h}+c}{2\bar{h}-c}\right)-c}\right] \tag{3}$$

$$s_{23,ex} = \frac{Eb}{48L^2}\left[\frac{c^3\left(2\bar{h}-c\right)}{\bar{h}\ln\left(\frac{2\bar{h}+c}{2\bar{h}-c}\right)-c}\right] \tag{4}$$

$$s_{26,ex} = \frac{Eb}{48L^2}\left[\frac{c^3\left(2\bar{h}+c\right)}{\bar{h}\ln\left(\frac{2\bar{h}+c}{2\bar{h}-c}\right)-c}\right] \tag{5}$$

$$s_{33,ex} = \frac{Eb}{192L}\left[\frac{\left(c^2-4\bar{h}^2\right)^2\ln\left(\frac{2\bar{h}+c}{2\bar{h}-c}\right)-4c\left(c^3-3c^2\bar{h}+4\bar{h}^3\right)}{\bar{h}\ln\left(\frac{2\bar{h}+c}{2\bar{h}-c}\right)-c}\right] \tag{6}$$

$$s_{36,ex} = \frac{Eb}{192L}\left[\frac{\left(4\bar{h}^2-c^2\right)\left(4\bar{h}c-\ln\left(\frac{2\bar{h}+c}{2\bar{h}-c}\right)\left(4\bar{h}^2-c^2\right)\right)}{\bar{h}\ln\left(\frac{2\bar{h}+c}{2\bar{h}-c}\right)-c}\right]. \tag{7}$$

where L is the beam member length; h_j and h_k are thicknesses at the 'j' and 'k' nodes, respectively; $\bar{h} = \frac{h_j+h_k}{2}$ is the average member thickness; $c = h_k - h_j$ is the tapering difference; E is the elasticity modulus; b is the beam width orthogonal to the beam plane; the varying thickness along the beam $h(\xi)$ is defined as: $h(\xi) = \bar{h} + c(\xi/L)$; and the cross-section moment of inertia is given by $I(\xi) = bh(\xi)^3/12$.

The above stiffness matrix is set in the local coordinate system of the beam member. Transferring into global Cartesian coordinates system is executed by multiplication with the rotation matrix. Denoting the node coordinates by $x_j,\ y_j,\ x_k,\ y_k$, the rotation matrix is formulated as:

$$L_x = x_k - x_j; \quad L_y = y_k - y_j; \quad L = \sqrt{L_x^2 + L_y^2}; \quad c_x = L_x/L; \quad c_y = L_y/L \tag{8}$$

$$\mathbf{R} = \begin{bmatrix} c_x & c_y & 0 \\ -c_x & c_y & 0 \\ 0 & 0 & 1 \end{bmatrix} \tag{9}$$

$$\mathbf{R}_t = \begin{bmatrix} \mathbf{R} & \mathbf{0} \\ \mathbf{0} & \mathbf{R} \end{bmatrix}. \tag{10}$$

Finally, the stiffness matrix of each member in global coordinates system is given by

$$\mathbf{K}_e = \mathbf{R}_t^T \mathbf{K}_m \mathbf{R}_t \tag{11}$$

2.2 Dealing with singularity for the prismatic case

The stiffness matrix formulation holds singularity in the prismatic case: $c = 0$, and small values of c lead to numerical instabilities. The optimization procedure relates the thicknesses of the beam member at its edges to the design variables, and the sensitivities are based on derivatives of the stiffness matrix. Therefore, the stiffness coefficients and their derivatives must not contain any discontinuity with respect to the tapering difference value c. Out of the various remedies the literature offers to this difficulty, we chose to implement the method suggested by Cleghorn and Tabarrok [1992]. It is based on switching to an approximate formulation near $c = 0$, by expanding the stiffness components to a Taylor series with respect to the tapering difference parameter c around zero. This method has the advantage of maintaining a simple analytical formulation in most of the beam tapering range on the one hand, and ensuring continuity in both the stiffness function and its derivatives on the other hand. As mentioned, the stiffness matrix is differentiated in the sensitivity analysis process, thus continuity of the first derivatives has to be guaranteed in the switching point between exact and approximate expressions. This condition is achieved by expanding the power series of the approximate formulation up to the second term, yielding

$$s_{11,ap} \approx \frac{bE}{L}\left(\bar{h} - \frac{1}{12\bar{h}}c^2\right) \tag{12}$$

$$s_{22,ap} \approx \frac{bE}{L^3}\left(\bar{h}^3 - \frac{3\bar{h}}{20}c^2\right) \tag{13}$$

$$s_{23,ap} \approx \frac{bE}{L^2}\left(\frac{\bar{h}^3}{2} - \frac{\bar{h}^2}{4}c - \frac{3\bar{h}}{40}c^2\right) \tag{14}$$

$$s_{26,ap} \approx \frac{bE}{L^2}\left(\frac{\bar{h}^3}{2} + \frac{\bar{h}^2}{4}c - \frac{3\bar{h}}{40}c^2\right) \tag{15}$$

$$s_{33,ap} \approx \frac{bE}{L}\left(\frac{\bar{h}^3}{3} - \frac{\bar{h}^2}{4}c - \frac{\bar{h}}{60}c^2\right) \tag{16}$$

$$s_{36,ap} \approx \frac{bE}{L}\left(\frac{\bar{h}^3}{6} - \frac{7\bar{h}}{120}c^2\right). \tag{17}$$

A smooth super-Gaussian window function is used for switching between exact and approximate formulations,

$$s_{mn} = (1 - w(c))\, s_{mn,ex} + w(c) s_{mn,ap};\ \ \forall m,n = 1...6;\ \ w(c) = exp\left(-\left|\frac{c}{\eta_c}\right|^{\beta}\right) \tag{18}$$

where η_c determines the neighborhood around $c = 0$ where switching to the approximate formulation is necessary. We used values around $\eta_c = 10^{-4}$ which have proven to work well, without further adjustments. Finally, β determines the smoothness of the switching window; it performs well with values in the range $10 < \beta < 50$. The continuity and smoothness of the approximation are shown in Figure 2.

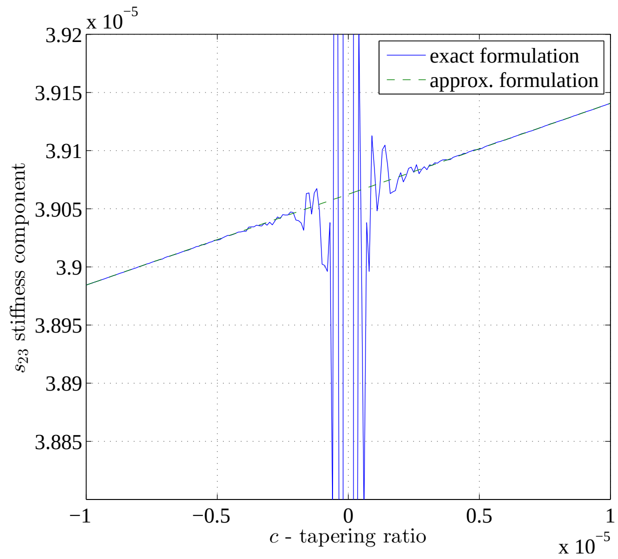

Figure 2: Analytical and approximate formulations of the s_{23} component of the stiffness matrix, in the vicinity of the prismatic case.

2.3 Ground structure parametrization

The ground structure is a well studied parametrization method used almost exclusively for truss layout optimization, as described in textbooks such as [Bendsøe and Sigmund, 2003] and references therein. Traditional ground structures have a connectivity index that allows overlapping of members as shown in Figure 3a. In truss structures such overlapping can be realized; however in the current context of imitating continuum-based design it is undesirable. Therefore, a ground structure enriched with nodes on all member intersections is suggested so to prevent overlapping, as shown in the Figure 3b.

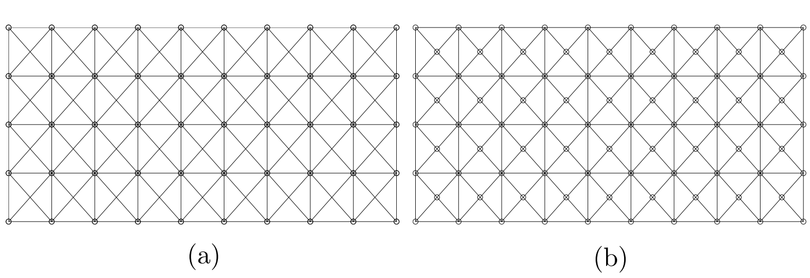

Figure 3: The ground structure parametrization, layout size: 10×5: (a) Traditional ground structure with overlapping connectivity to the nearest node (b) Enriched nodes ground structure without overlapping.

2.4 Beam formulation based on static condensation

Static condensation is a well-known technique that is typically used for reducing the order of a static problem. A detailed description of this method can be found in the FEM and the structural analysis literature, as in [Bathe, 2006] as well as in [Weaver and Gere, 2012]. The condensed beam in the case discussed herein consists of a sequence of three linear tapered beam segments, whose formulation was discussed above. The assembled 12×12 stiffness matrix of this sequence is rearranged such that internal *free* degrees of freedom (DOF) designated with the subscript f, and external *restrained* DOF designated with the subscript r, are aggregated such that the static equation of a single condensed beam becomes:

$$\begin{bmatrix} \mathbf{K}_{ff} & \mathbf{K}_{fr} \\ \mathbf{K}_{rf} & \mathbf{K}_{rr} \end{bmatrix} \begin{bmatrix} \mathbf{U}_f \\ \mathbf{U}_r \end{bmatrix} = \begin{bmatrix} \mathbf{F}_f \\ \mathbf{F}_r \end{bmatrix} \tag{19}$$

where the vectors $\mathbf{U}_r$, $\mathbf{F}_r$ contain the displacements and loads of the external DOF respectively, while $\mathbf{U}_f$, $\mathbf{F}_f$ contain the internal displacements and loads respectively. Considering zero internal loads inside the beam, i.e. $\mathbf{F}_f = \mathbf{0}$, the internal displacements can be expressed as a function of the external displacements,

$$\mathbf{U}_f = -\mathbf{K}_{ff}^{-1}\mathbf{K}_{fr}\mathbf{U}_r. \tag{20}$$

Substituting into the second row of (19) yields:

$$\left(-\mathbf{K}_{rf}\mathbf{K}_{ff}^{-1}\mathbf{K}_{fr} + \mathbf{K}_{rr}\right)\mathbf{U}_r = \mathbf{F}_r. \tag{21}$$

Equation (21) is now the condensed static problem to be solved and the term in the parentheses is considered the *condensed stiffness matrix.*

The motivation for utilizing static condensation as a method for the beam-based formulation is the enhancement of the design space and the design freedom, with only a limited additional computational cost. As mentioned above, each of the three segments is formulated as a linear tapered beam, as illustrated in Figure 4. The inner segment shares its nodal thicknesses with its two neighboring side segments. The sizing of the condensed beam is therefore determined by four thickness values that are associated with physical design variables. In the current implementation, the outer segments have equal length determined according to a partitioning ratio r_L, that is the ratio between the length of the side segments and the length of the whole beam: $L_1 = L_3 = r_L L$, $L_2 = (1-2r_L)L$. Adding this ratio as another design variable can be considered as a future enhancement. This formulation requires to cautiously derive consistent sensitivity analysis for both shape and sizing variables, as will be detailed in the next section.

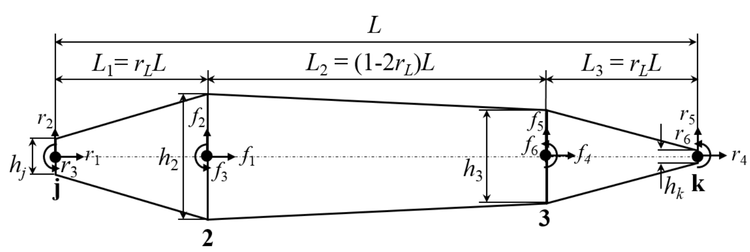

Figure 4: A condensed beam consisting of three tapered segments. The external nodes are denoted j, k; the internal nodes are 2, 3; the four thicknesses are h_j, h_k, h_2, h_3; and the designated internal (free) and external (restrained) DOF are $f_1, ..., f_6$; $r_1, ..., r_6$.

3 Beam-based shape and sizing-topology optimization

The limited design freedom of the discrete parametrization is further enhanced by utilizing two optimization phases of shape and sizing-topology. The two optimization phases are applied on the enriched ground structure discussed above. We employed the alternating approach suggested by Ben-Tal et al. [1993] and later developed and examined by Achtziger [2007]. The overall workflow of the optimization scheme is presented in Figure 5.

Achtziger [2007] demonstrated how an alternating scheme with orthogonal shape and sizing design updates can terminate with no solution. The suggested remedy is the formulation of a 'master-slave' relation where the shape phase is updated only after the sizing phase converged to a global minimum. Applying such a scheme is possible for a truss-based ground structure as shown by Gil and Andreu [2001]. In each sizing optimization phase, global optimality is guaranteed – this is a well-known attribute of the truss sizing problem. However, for a beam-based ground structure global optimality for the sizing phase cannot be guaranteed. Thus herein we resort to using a simple numerical convergence criterion. Though it might be considered heuristic, numerical experiments have demonstrated satisfactory results.

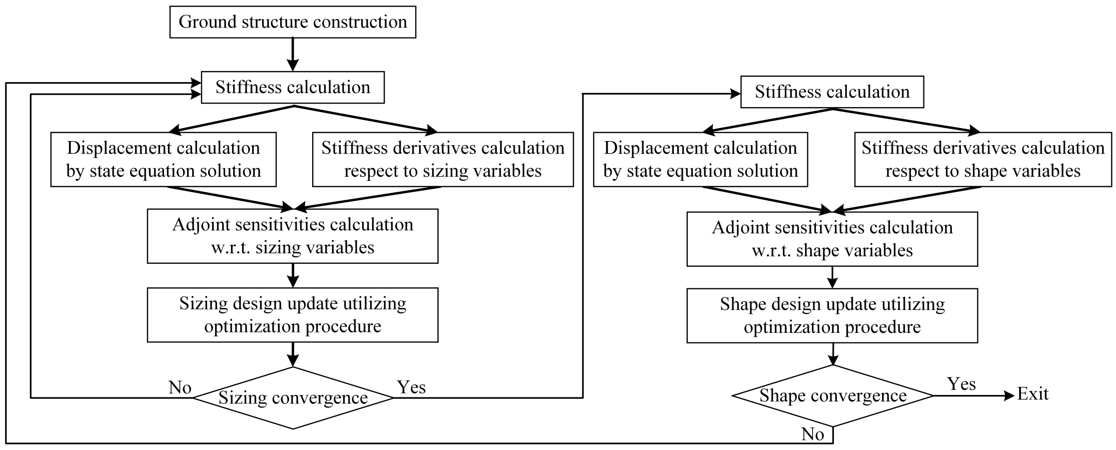

Figure 5: Description of the alternating master-slave optimization process with both shape and sizing-topology phases.

3.1 Shape optimization problem formulation

The shape optimization phase is performed according to the following problem formulation:

$$\begin{aligned} \min_{\mathbf{x}} \quad & f(\mathbf{x}) \\ \text{s.t.} \quad & \sum_{i=1}^{nm} b\bar{h}_i L_i(\mathbf{x}) - V^\star \leq 0 \\ & \mathbf{A}_d\mathbf{x} - \mathbf{b} \leq 0 \\ & \mathbf{x}_{min} \leq \mathbf{x} \leq \mathbf{x}_{max} \\ \text{with:} \quad & \mathbf{K}(\mathbf{x})\mathbf{u} = \mathbf{p}. \end{aligned} \tag{22}$$

The objective function is $f(\mathbf{x})$, that in the current context represents either compliance or a certain target displacement; nm is the number of members in the ground structure; b is the thickness of the 2-D domain; $\bar{h}_i$ is the mean thickness of the i-th member; $L_i(\mathbf{x})$ is the length of the i-th member, that depends explicitly on the shape variables; $V^\star$ is the available volume; $\mathbf{A}_d$ and $\mathbf{b}$ are the linear adjacency operator and the nodes adjacency constraints vector respectively, that ensure the coordinated movement of adjacent nodes, as will be discussed in detail below; and $\mathbf{x}_{min}$ and $\mathbf{x}_{max}$ are global box constraints for the positions of the nodes. The vector of design variables $\mathbf{x}$ contains the coordinates of all nodes in 2-D, therefore it has the size of $2\times$[number of nodes]. The optimization problem is formulated following the nested approach, meaning that the static equilibrium equations are solved separately, where $\mathbf{p}$ is the external load vector; $\mathbf{K}$ is the stiffness matrix; and $\mathbf{u}$ is the displacements vector.

The construction of the linear constraints set starts by defining a neighborhood with a fixed radius R_n prior to the optimization in the initial ground structure, as shown in Figure 6. The value of R_n determines how many nodes are associated in the constraints set, and therefore it affects the regularity level of the structure. Two design variables x_l and x_m denote the same type of coordinate (i.e. either X or Y in 2-D) of two different nodes: a specific node l and its current neighbor m. The value of the relevant entry in $\mathbf{A}_d$ is computed as follows:

$$A_{d_{l,m}} = \begin{cases} -1, & \text{if } l = m. \\ 1, & \text{if } l \neq m \text{ and } r_{l,m} \leq R_n \\ 0, & \text{otherwise} \end{cases} \tag{23}$$

The position of any neighboring node m with respect to a specific node l is bounded between $b_{l,min}$ and $b_{l,max}$ as illustrated in Figure 6. These values are the entries of $\mathbf{b}$ in the relevant row and sign. Thus, the inequality size is twice the number of interactions between nodes, as determined by the size of R_n. Once for all $b_{l,min}$ and once for all $b_{l,max}$.

We chose the Sequential Linear Programming (SLP) to solve the shape optimization phase because its capability of handling a large set of linear constraints with little effect on the computational burden. In an SLP procedure, a sub problem is formulated within each design iteration, based on a linearization of the objective function with respect to the design variables, inside predetermined move limits. The sub problem is solved by a standard interior-point Linear Programming solver in MATLAB. The advantage of using SLP for the shape optimization phase is discussed further in Section 3.4.

3.2 Sizing-topology optimization problem

The sizing-topology optimization formulation is similar to the traditional truss ground structure sizing problem with a volume constraint, as discussed in structural and topology optimization literature [e.g. Bendsøe and Sigmund, 2003, Christensen and Klarbring, 2009]. Unlike the truss-based ground structure characterized by a single design variable for each member, herein the design space is enhanced by using one of the following two formulations:

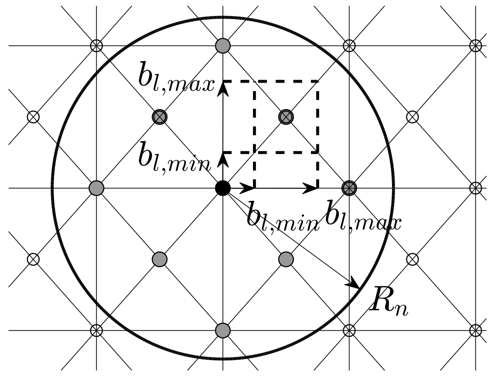

Figure 6: A specific node l (black), its neighboring nodes (gray), and the bounds $b_{l,min}$ and $b_{l,max}$ constraining neighbors movement.

1. Each member is a linear tapered beam as illustrated in Figure 1:

$$\begin{aligned} \min_{\boldsymbol{\rho}} \quad & f(\boldsymbol{\rho}) \\ \text{s.t.} \quad & g(\boldsymbol{\rho}) = \sum_{i=1}^{nm} b\bar{h}_i(\rho_{2i-1}, \rho_{2i}) L_i - V^\star \leq 0 \\ & \boldsymbol{\rho}_{min} \leq \boldsymbol{\rho} \leq \boldsymbol{\rho}_{max} \\ \text{with:} \quad & \mathbf{K}(\boldsymbol{\rho})\mathbf{u} = \mathbf{p} \end{aligned} \tag{24}$$

The vector of design variables $\boldsymbol{\rho}$ contains scaled mathematical variables that for this formulation relate to the thicknesses of each i-th member end nodes j and k:

$$h_{i_j} = h_{2i-1} = h_{min} + (h_{max} - h_{min})\rho_{2i-1} \tag{25}$$
$$h_{i_k} = h_{2i} = h_{min} + (h_{max} - h_{min})\rho_{2i} \tag{26}$$
$$\bar{h}_i = (h_{2i-1} + h_{2i})/2 \tag{27}$$

2. Each member is composed of three linear tapered beam segments as shown in Figure 4:

$$\begin{aligned} \min_{\boldsymbol{\rho}} \quad & f(\boldsymbol{\rho}) \\ \text{s.t.} \quad & g(\boldsymbol{\rho}) = \sum_{i=1}^{nm} b\bar{\mathbf{h}}_i(\rho_{4i-3}, ..., \rho_{4i})^T \mathbf{L}_i - V^\star \leq 0 \\ & \boldsymbol{\rho}_{min} \leq \boldsymbol{\rho} \leq \boldsymbol{\rho}_{max} \\ \text{with:} \quad & \mathbf{K}(\boldsymbol{\rho})\mathbf{u} = \mathbf{p} \end{aligned} \tag{28}$$

where the mean thicknesses and lengths of the internal segments are defined as:

$$\bar{\mathbf{h}}_i^T = \left[\bar{h}_{i,1}, \bar{h}_{i,2}, \bar{h}_{i,3}\right]^T \tag{29}$$
$$\bar{h}_{i,1} = (h_{4i-3} + h_{4i-2})/2 \tag{30}$$
$$\bar{h}_{i,2} = (h_{4i-2} + h_{4i-1})/2 \tag{31}$$
$$\bar{h}_{i,3} = (h_{4i-1} + h_{4i})/2 \tag{32}$$
$$\mathbf{L}_i = [L_{i_1}, L_{i_2}, L_{i_3}]^T. \tag{33}$$

This formulation utilizes static condensation as discussed above. The four thicknesses of each i-th member are related to the scaled design variables: $\rho_{4i-3}, ..., \rho_{4i}$, with the same relation as in the single tapered beam formulation. This formulation doubles the size of the sizing-topology design space and therefore enhances the design freedom.

In the context of the objective function, we used two alternatives for the functional dependency of the physical variable –namely the thickness h of a beam cross-section at a certain point–on its corresponding mathematical design variable ρ:

1. *A linear function dependency:*

$$h(\rho) = h_{min} + (h_{max} - h_{min})\rho. \tag{34}$$

With this setting, the design variables can reach zero values. For allowing topological design changes, h_{min} needs to attain a very small value. Then, when the mean thickness of the member reaches h_{min}, it may be considered as an eliminated member, thus a topological change occurs. Nonetheless, as with continuum topology optimization, the small member stiffness is still considered in the state equation for numerical purposes and no reconstruction of the ground structure is performed.

2. *A penalized function dependency:* Although the linear function is capable of controlling the structural topology, this setting does not always succeed in eliminating all thin members, as demonstrated in Figure 8b. The difficulty with eliminating thin members was also observed by Ramos Jr and Paulino [2016] who suggested a discrete filtering process. In a different context, Groen and Sigmund [2017] used a smooth Heaviside function to filter out small details in microstructural layouts. A penalizing projection function is formulated using a Sigmoid function with a threshold value to improve the so-called topological decision. Then the stiffness is evaluated by the penalized thickness while the volume is related to the linear thickness. Hence thickness values in the penalized range are not beneficial. Similarly to many other filtering methods, this projection function uses a *mathematical* thickness $h = h_{max}\rho$ and projects it onto a *physical* thickness $\tilde{h}$, while penalizing all thicknesses below the predefined minimum thickness h_{min}. For preventing an ill-conditioned structural analysis, a small minimum value is maintained for penalized thicknesses, $h_\epsilon = 10^{-9}$. We found that with the Sigmoid function the optimization process is more stabilized with less tendency to oscillate compared to other filtering methods. The continuous penalization procedure herein utilizes the aforementioned smooth differentiable Sigmoid function, given by the following expressions (see also Figure 7):

$$\begin{aligned} h(\rho) &= h_{max}\rho \\ \tilde{h}(\rho) &= h_\epsilon + S\left(h(\rho), h_{min}, h_{max}, \beta_s\right) \\ S\left(h, h_{min}, h_{max}, \beta_s\right) &= \frac{h\left[1 + e^{-\beta_s\left(\frac{1-h_{min}}{h_{max}}\right)}\right]}{1 + e^{-\beta_s\left(\frac{h-h_{min}}{h_{max}}\right)}}. \end{aligned} \tag{35}$$

The value of β_s serves as the projection sharpness factor. A low value of β_s typically results in a minor influence of the penalization. Then some thin members are maintained with intermediate thickness, resulting in an inconsistent structure. Using high values of β_s may cause the optimization to oscillate. It was found through numerical testing that a value in the range $[8, 64]$ leads to satisfactory results, as demonstrated on Figures 7 to 9. A continuation approach that updates β_s gradually every few iterations is utilized in order to avoid divergence of the optimization.

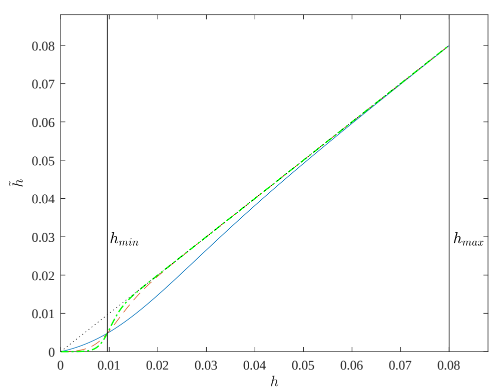

Figure 7: Sigmoid penalty function of a mathematical thickness h projected to a physical thickness $\tilde{h}$. $h_{max} = 0.08, h_{min} = 0.0096$ $\beta_s = 8$ solid blue, $\beta_s = 32$ dashed red, $\beta_s = 64$ dash-dotted green. The dotted line is the $h = \tilde{h}$ line.

Figures 8b and 8d present the optimized layouts of a fixed cantilever beam with a concentrated load on the far end corner. The setup of the problem is illustrated in Figure 8a. A 6×3 grid is used for the ground structure. Clearly, with the penalized function (Figure 8d, and Figure 8c with the complete underlying ground structure), the optimized layout exhibits a cleaner and more regularized topology, compared to the result with a linear dependency without penalization (Figure 8b). This shows the benefit of using the penalization (35) for obtaining clear topological designs using beam layouts.

Figure 9 illustrates the influence of the Sigmoid penalty function. The circles laying on the penalty function plot are the optimized thicknesses of the cantilever beam problem. The thicknesses are either distributed above h_{min} or concentrated at h_ϵ, meaning they are practically eliminated from the structural layout.

3.3 Sensitivity analysis

Adjoint sensitivity analysis is used for computing the derivatives of functionals involving state variables. We consider two objective functionals of this type: 1) Minimum compliance design, i.e. $f = \mathbf{p}^T\mathbf{u}$, where $\mathbf{p}$ is the external force vector (considered to be design independent) ; 2) Maximize the output displacement of a compliant mechanism, i.e. $f = \mathbf{l}^T\mathbf{u}$, where $\mathbf{l}$ is a unit vector whose value is 1 at the output degree of freedom and zero elsewhere. For the minimum compliance problem, the adjoint vector is identical to the displacement vector: $\boldsymbol{\lambda} \equiv \mathbf{u}$. For the output displacement problem, the adjoint vector is the solution of the linear system $\mathbf{K}^T\boldsymbol{\lambda} = \mathbf{l}$. Once the adjoint vector is determined, the derivative is computed for each design variable as $\frac{\partial \hat{f}}{\partial z_i} = -\boldsymbol{\lambda}^T\frac{\partial \mathbf{K}}{\partial z_i}\mathbf{u}$. Specific details regarding the term $\frac{\partial \mathbf{K}}{\partial z_i}$ are provided in the following.

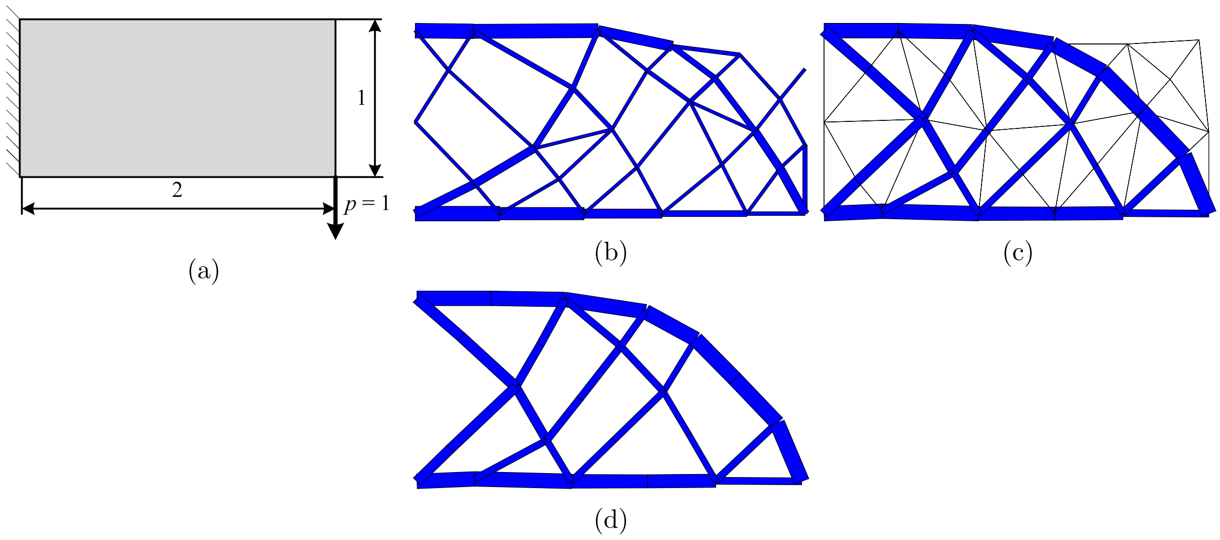

Figure 8: Demonstrative minimum compliance optimization of a cantilever beam: (a) Problem setup, grid: 6×3, $V^{\star} = 0.3V$, $h_{min} = 0.0096$, $h_{max} = 0.08$; (b) Linear dependency between design variables and beam thicknesses without penalization; (c) Penalized dependency between design variables and beam thicknesses, complete ground structure is presented; (d) Same as (c) but without displaying the penalized members.

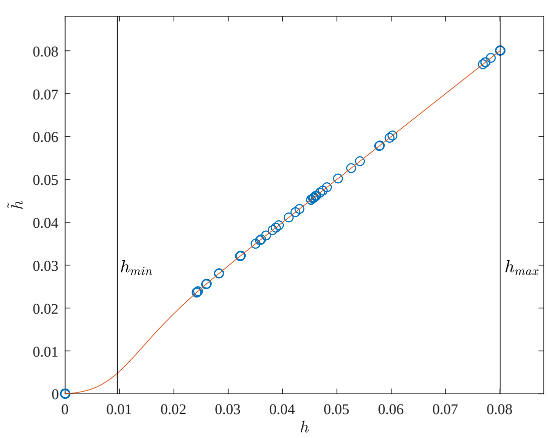

Figure 9: Optimized member thicknesses of the above 6×3 cantilever problem, laying on the Sigmoid penalty function plot with $\beta_s = 20$.

3.3.1 Differentiation with respect to shape variables

As mentioned above, the shape design variables are simply the node coordinates. Because each node is connected to more than one member, an assembly summation is applied to collect the contributions of sensitivities from all members connected to a certain node. For the objective functional we have

$$\frac{\partial f}{\partial z_i} = -\sum_{e \in N_i} \boldsymbol{\lambda}_e \frac{\partial \mathbf{K}_e}{\partial z_i} \mathbf{u}_e \tag{36}$$

where z_i represents any node coordinate at the end of a member, $z_i = \{x_j, x_k, y_j, y_k\}$ and N_i is the set of members e connected to the node. In relation to Eq. (11), the derivative of a member stiffness matrix with respect to a certain design variable is given by

$$\frac{\partial \mathbf{K}_e}{\partial z_i} = \frac{\partial}{\partial z_i}\left(\mathbf{R}_t^T \mathbf{K}_m \mathbf{R}_t\right) = \frac{\partial \mathbf{R}_t^T}{\partial z_i} \mathbf{K}_m \mathbf{R}_t + \mathbf{R}_t^T \frac{\partial \mathbf{K}_m}{\partial z_i} \mathbf{R}_t + \mathbf{R}_t^T \mathbf{K}_m \frac{\partial \mathbf{R}_t}{\partial z_i}. \tag{37}$$

Then, the the stiffness matrix derivatives in local coordinates and of the rotational matrix are

$$\frac{\partial \mathbf{K}_m}{\partial z_i} = \frac{\partial \mathbf{K}_m}{\partial L_m} \frac{\partial L_m}{\partial z_i} \tag{38}$$

$$\frac{\partial \mathbf{R}_t}{\partial z_i} = \frac{\partial \mathbf{R}_t}{\partial L_m} \frac{\partial L_m}{\partial z_i} + \frac{\partial \mathbf{R}_t}{\partial L_z} \frac{\partial L_z}{\partial z_i}; \ \forall z = x, y \tag{39}$$

where L_m is the length of the particular member. Finally, the explicit components of these derivatives are straightforward based on Eqs. (8) through (11).

As for the volume constraint in the shape optimization problem (22), it involves only straightforward derivatives of the member length L_m with respect to a certain node coordinate. These again are found based on the relations in Eq. (8).

3.3.2 Differentiation with respect to sizing-topology variables

In the following we will consider the explicit derivatives with respect to a certain sizing-topology variable denoted ρ_n, that corresponds to the cross-section thickness at a certain point. As opposed to the case of shape variables, the rotation matrix does not depend on the design, giving

$$\frac{\partial \mathbf{K}_e}{\partial \rho_n} = \mathbf{R}_t^T \frac{\partial \mathbf{K}_m}{\partial \rho_n} \mathbf{R}_t. \tag{40}$$

Based on the switching between exact and approximate stiffnesses according to Eq. (18), the stiffness matrix derivative is given by

$$\frac{\partial \mathbf{K}_m}{\partial \rho_n} = \frac{\partial \mathbf{K}_{m,ex}}{\partial \rho_n}(1-w) - \mathbf{K}_{m,ex}\frac{\partial w}{\partial \rho_n} + \frac{\partial \mathbf{K}_{m,ap}}{\partial \rho_n} w + \mathbf{K}_{m,ap}\frac{\partial w}{\partial \rho_n} \tag{41}$$

The switching window function $w(c)$ is characterized by zero derivatives in all the range except near $(-\eta_c, \eta_c)$ where the transition from zero to one occurs. However, due to the continuity requirement, the value of η_c is chosen such that at $c(\rho_n) = \pm\eta_c$, we have $\mathbf{K}_{m,ex} = \mathbf{K}_{m,ap}$. Hence, the general form of derivative can be reduced to:

$$\frac{\partial \mathbf{K}_m}{\partial \rho_n} = \frac{\partial \mathbf{K}_{m,ex}}{\partial \rho_n}(1-w) + \frac{\partial \mathbf{K}_{m,ap}}{\partial \rho_n} w. \tag{42}$$

The derivatives of the local stiffness matrix depend on the relation between the effective thickness and the underlying mathematical design variable. For the linear dependency as in Eq. (34) we have

$$\frac{\partial \mathbf{K}_m}{\partial \rho_n} = \left(\frac{\partial \mathbf{K}_m}{\partial \bar{h}} \frac{\partial \bar{h}}{\partial h_n} + \frac{\partial \mathbf{K}_m}{\partial c} \frac{\partial c}{\partial h_n} \right) \frac{\partial h_n}{\partial \rho_n} \tag{43}$$

$$\frac{\partial h_n}{\partial \rho_n} = h_{max} - h_{min} \tag{44}$$

whereas the expressions for $\frac{\partial \mathbf{K}_m}{\partial \bar{h}}$ and $\frac{\partial \mathbf{K}_m}{\partial c}$ can be deduced from Eqs. (2) through (7) and Eqs. (12) through (17). Furthermore, the expressions for $\frac{\partial \bar{h}}{\partial h_n}$ and $\frac{\partial c}{\partial h_n}$ are straightforward based on the linear tapering.

In a similar manner, when the thickness is penalized according to Eq. (35), h_n serves as an intermediate variable while $\tilde{h}_n$ is the actual thickness, yielding

$$\frac{\partial \mathbf{K}_m}{\partial \rho_n} = \left(\frac{\partial \mathbf{K}_m}{\partial \bar{h}} \frac{\partial \bar{h}}{\partial \tilde{h}_n} + \frac{\partial \mathbf{K}_m}{\partial c} \frac{\partial c}{\partial \tilde{h}_n} \right) \frac{\partial \tilde{h}_n}{\partial h_n} \frac{\partial h_n}{\partial \rho_n} \tag{45}$$

$$\frac{\partial \tilde{h}_n}{\partial h_n} = \frac{\partial S}{\partial h_n} = \frac{\left[1 + e^{-\beta\left(\frac{1-h_{min}}{h_{max}}\right)} \right] \left[\left(\frac{\beta h_n}{h_{max}} + 1 \right) e^{-\beta\left(\frac{h_n - h_{min}}{h_{max}}\right)} \right]}{\left[e^{-\beta\left(\frac{h_n - h_{min}}{h_{max}}\right)} \right]^2} \tag{46}$$

$$\frac{\partial h_n}{\partial \rho_n} = h_{max} \tag{47}$$

The volume constraint derivatives are obtained directly from the problem formulations (22), (24), (28) without penalization. For the case of a linearly tapered beam as in (24), the derivative with respect to the underlying mathematical variable is given by

$$\frac{\partial g}{\partial \rho_n} = \frac{b L_m}{2}(h_{max} - h_{min}) \tag{48}$$

where L_m is the beam member length which one of its ends sections is controlled by ρ_n.

3.3.3 Sensitivity analysis of the condensed beam formulation

In formulation (28), static condensation is used for deriving the member stiffness matrix in local coordinates. We calculate the sensitivities by differentiation of the full 12×12 stiffness matrix from Eq. (19). It was found through numerical tests that utilizing direct differentiation of the condensed stiffness matrix from (21) can become ill-conditioned for penalized thin members, presumably because this formulation involves the quadratic-inverse term: $\frac{\partial \mathbf{K}_{ff}^{-1}}{\partial z_i} = -\mathbf{K}_{ff}^{-1} \frac{\partial \mathbf{K}_{ff}}{\partial z_i} \mathbf{K}_{ff}^{-1}$.

In the solution of the equilibrium and adjoint equations, the displacements and adjoint variables of the external DOF, $\mathbf{u}_r$ and $\boldsymbol{\lambda}_r$ are found. Then the displacements and adjoint variables of the internal (condensed) DOF are computed on the member level:

$$\mathbf{u}_f = -\mathbf{K}_{ff}^{-1} \mathbf{K}_{fr} \mathbf{u}_r \tag{49}$$

$$\boldsymbol{\lambda}_f = -\mathbf{K}_{ff}^{-1} \mathbf{K}_{fr} \boldsymbol{\lambda}_r. \tag{50}$$

Thus, the full displacements and the full adjoint vectors of each composed member are obtained:

$$\mathbf{u}_e = \begin{bmatrix} \mathbf{u}_f \\ \mathbf{u}_r \end{bmatrix} \tag{51}$$

$$\boldsymbol{\lambda}_e = \begin{bmatrix} \boldsymbol{\lambda}_f \\ \boldsymbol{\lambda}_r \end{bmatrix}. \tag{52}$$

The result can be plugged in to the sensitivity expression for a full composed member e that has 12 DOF,

$$\frac{\partial f}{\partial z_i} = -\boldsymbol{\lambda}_e \frac{\partial \mathbf{K}_e}{\partial z_i} \mathbf{u}_e \tag{53}$$

where z_i represents a generic design variable. The derivatives of each part of the stiffness matrix $\mathbf{K}_e$ can be obtained based on the previous subsections, composing the complete derivative

$$\frac{\partial \mathbf{K}_e}{\partial z_i} = \begin{bmatrix} \frac{\partial \mathbf{K}_{ff}}{\partial z_i} & \frac{\partial \mathbf{K}_{fr}}{\partial z_i} \\ \frac{\partial \mathbf{K}_{rf}}{\partial z_i} & \frac{\partial \mathbf{K}_{rr}}{\partial z_i} \end{bmatrix} \tag{54}$$

where the same approach is used for both shape and sizing-topology sensitivity analysis.

The volume constraint sensitivities in the case of the condensed beam are derived similarly to (48) based on Eqs. (29) through (33). Yet, they are calculated for each segment instead of the whole member. Finally, the formulations of both shape and sizing-topology sensitivity analysis have been verified by comparison to finite differences.

3.4 Solution procedures

Two of the most common gradient-based methods for solving structural optimization problems are Optimality Criteria (OC) procedures and the Method of Moving Asymptotes (MMA, [Svanberg, 1987]). OC procedures can be very efficient for problems such as minimum compliance because the volume constraint is a continuously decreasing function of the Lagrange multiplier [e.g. Bendsøe and Sigmund, 2003]. However, for the shape optimization phase and for problems such as the compliant mechanism this is not the case. Thus, more general procedures such as MMA or other mathematical programming methods must be utilized [Bendsøe and Sigmund, 2003]. The MMA method gained high popularity in structural optimization, particularly for density-based topology optimization, and it can efficiently solve relatively complex problems. However, MMA may not be suitable for handling problems such as (22) because of the presence of a large set of linear constraints. In such cases, generic mathematical programming procedures such as Sequential Linear Programming (SLP) or Sequential Quadratic Programming (SQP) can be more suitable. Therefore, the presented beam-based optimization scheme with shape and sizing-topology optimization phases utilizes SLP for the shape optimization phase and either OC or MMA for the sizing-topology optimization phase.

4 Comparison to continuum optimization

The main purpose of this article is to suggest a computationally cheap alternative to continuum topology optimization. An essential step in the evaluation of the beam-based formulation is its consistent and fair comparison against state-of-the-art continuum topology optimization procedures. We address this issue in this section. First we focus on the transformation of the results to a continuum model and then on the determination of the appropriate length scale for comparison to continuum procedures.

4.1 Projection to the continuum domain

Comparison of the optimized beam-based layouts with a compatible solution obtained by a continuum approach must be performed in the continuum domain. For this purpose, the discrete optimized layout is projected into a continuum domain by means of simple image processing tools. The objective function is then computed on the continuum model for fairly comparing it to standard continuum-based optimization. We note that the projection can be utilized also as a starting point for further optimization iterations in the continuum domain. Hence, the beam-based optimization approach can be viewed as a coarse optimization stage or as an *educated guess* inherited by a more fine-tuned optimization stage in the continuum domain.

The steps of the continuum projection are detailed hereby and illustrated in Figure 10 on a half-MBB beam example:

1. Executing the beam-based optimization and obtaining the optimized layout (Figure 10a), plotted with true member sizes.

2. 'Patching' the layout with filled circles to eliminate notches between members near the nodes and with filled squares on the supports (Figure 10b). The patch size is determined by the thickest member attached to the node.

3. Printing of the patched layout to an image, while cropping its margins to assure that material will possess the proper domain so boundary conditions and loads can be applied.

4. Reading the printed image into a matrix of density values, with a predefined resolution that corresponds to the required length scale (Figure 10c). The procedure for determining the appropriate length scale is discussed below.

5. Applying the commonly used density filter [Bruns and Tortorelli, 2001, Bourdin, 2001]. The filter radius is set to capture the dictated length scale, as discussed below. The margins of the domain are padded with extra elements for more consistent filtering around the domain margins [Lazarov et al., 2016, Lazarov and Wang, 2017, Clausen and Andreassen, 2017], see Figure 10d.

6. Applying a Heaviside projection with a predefined threshold and sharp transition to ensure crisp void-material separation as suggested in [Wang et al., 2011] with $\eta = 0.5$ and $\beta = 100$ (Figure 10e).

7. Applying loads and supports and solving the finite element analysis on the projected continuum domain, yielding an evaluation of the objective function.

The sequence of operations described above can be easily performed using standard numerical libraries, in this particular work we implemented the procedure in MATLAB [MATLAB, 2013].

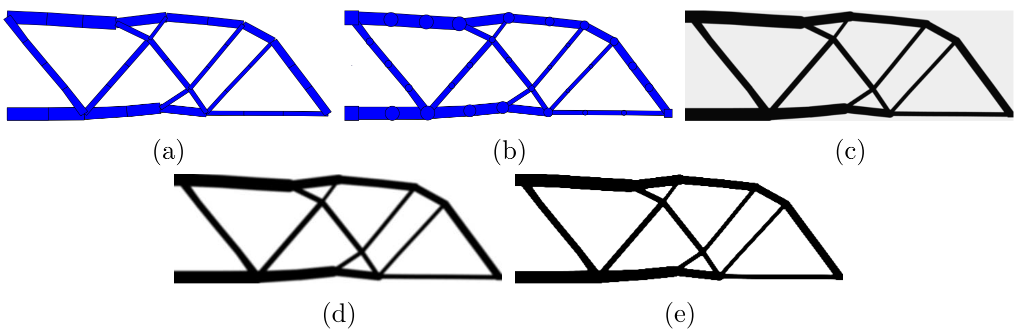

Figure 10: Illustration of the continuum projection process. (a) Result of the beam-based optimization. (b) Patching nodes, supports and loading positions. (c) Reading the printed layout in a resolution determined by the minimum length scale; each pixel represents a single finite element. (d) Applying density filtering. (e) Applying Heaviside projection.

Members tend to overlap in the vicinity of the joints. A 2-D projection eventually flattens those stacks, thus the calculated volume fraction of the projected continuum layout is lower than the volume fraction of the discrete layout. The compared volume fraction on the benchmark examples is always the smaller volume fraction, determined by the continuum projection layout.

4.2 Determining an appropriate length scale

In the beam-based optimization scheme, the minimum length scale is determined explicitly by the minimum thickness of members, h_{min}. This parameter is predefined in the optimization definitions and it can be related directly to manufacturing constraints, such as resolution limitation of an AM facility. In contrast, determining an appropriate length scale for the continuum approach is not as straightforward.

The suggested definition for the normalized minimum length scale in [Wang et al., 2011] is adopted for determining the continuum resolution in the projection stage of the beam-based optimization scheme. Specifically, we refer to Figure 12 for defining the relation between the length scale, the filter radius and the projection threshold η. Given the minimum thickness h_{min} and a predefined dilated design threshold η_{dil}, one can determine the physical size of the filter radius, R_{phys}. For a valid finite element analysis, we require that R_{phys} covers at least 3 finite elements and this dictates the minimum resolution for a comparative continuum-based optimization. For example: for a specified $\eta_{dil} = 0.4$ and a minimum thickness (or length scale) $h_{min} = 0.0118L$, according to Figure 12 in Wang et al. [2011], the actual ratio complies with the relation: $h_{min}/2R_{phys} \approx 0.31$ such that the physical radius covers three elements. This gives the necessary value of $R_{phys} = h_{min}/0.62 = 0.0188L$. Hence, the element size is set to: $a_{FE} = R_{phys}/3 = 0.00625L$, and the resolution is: round $\{L/a_{FE} = 1/0.00625\} = 160$ elements.

The beam-based approach allows to specify also the maximum length scale explicitly simply by setting the value for the maximum thickness h_{max}. It is common to have a reasonable ratio between minimum and maximum thicknesses in the range of: $[0.1, 0.3]$ for the reasons of structural robustness and restructurability. As mentioned in the introduction, the maximum length scale affects the design redundancy and the capability to impose it explicitly will be demonstrated in the examples section.

5 Numerical examples

In this section, we present several results obtained with the beam-based optimization. First, we examine classical benchmark problems – minimum compliance design of an MBB-beam and compliant mechanism design. The two examples include a detailed comparison to continuum-based solutions. Subsequently, we demonstrate the capability to explicitly enforce a maximum length scale on the design. The section concludes with examples of high resolution designs with pseudo meso-scale members obtained efficiently due to the beam representation.

5.1 Minimum compliance of the MBB-beam

In this example we examine the classical MBB-beam problem (see setup in Figure 11). The optimization is performed on a symmetric half of the domain with the dimensions 3×1, discretized by an enriched ground structure with 9×3 nodes. The problem is solved with two volume fraction constraints: $v_f = 0.3, 0.5$; and with two beam parameterizations: the linear tapered beam and the three segments condensed beam. The shape adjacency constraints are set to $b_{l,min} = 0.2$ and $b_{l,max} = 2$ with respect to one cell side size of the ground structure. The penalization function sharpness parameter is set to $\beta_s = 32$ and a penalty continuation is applied. The minimum and maximum thicknesses are $h_{min} = 0.0118$ and $h_{max} = 0.125$, respectively. For the condensed beam representation, the length ratio of the internal members is set to $r_L = 1/3$, stating that the condensed beam consists of three equal-length segments.

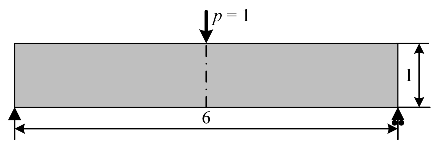

Figure 11: Dimensions, boundary conditions and loading for the MBB beam optimization problem.

The performance of the beam-based optimization approach is compared to the robust topology optimization method of Wang et al. [2011]. The dilated design is defined by the threshold value of $\eta_{dil} = 0.4$ and the corresponding eroded design is defined by $\eta_{ero} = 1 - \eta_{dil} = 0.6$. A penalty continuation approach is used in order to deal better with the high resolution domain, as suggested in [Bendsøe and Sigmund, 1999]. The necessary resolution of the continuum domain is found to be 480×160 with the filter radius spanning 3 elements.

Table 1 provides a comprehensive presentation of the results and their comparison to continuum topology optimization. In the first two rows, the design is superimposed on the complete ground structure including the eliminated members, to demonstrate the effect of shape optimization. Clearly, for the low volume constraint the optimization of both beam formulations converged to the same topology with similar results. Designs with low volume constraint consists mainly on members contributing tensile and compression stiffnesses. Thus, a 'truss-like' layout is obtained on both formulations. The corresponding continuum solution obtained similar values, though the layouts of both beam formulations appear to be more regularized. When a higher volume constraint is imposed, the results demonstrate a more complex load transfer. The optimized designs contain therefore several thick and tapered members in both beam formulations. Both beam-based formulations reached slightly higher compliance than the continuum approach, presumably because of its inherent design freedom limitation.

Nevertheless, the superior performance of the beam-based approach with respect to computational time is evident. The total run times of the beam-based optimization were in the range of 11% to 21% of the run times required for continuum optimization. This reveals the potential of the proposed approach as a cheap alternative to continuum topology optimization.

5.2 Compliant mechanism design

In this example, we design a compliant mechanism that maximizes the output of a negative displacement, see Figure 12 for the problem setup. This can be achieved by simply minimizing the displacement at the output DOF.

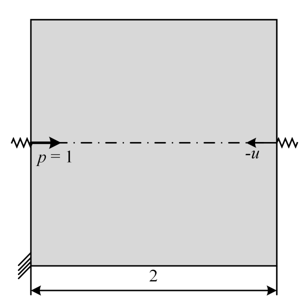

Figure 12: Boundary conditions and loading for the compliant mechanism design problem

The beam-based approach is executed on a domain of 2×1 which is discretized by an enriched ground structure with 4×3 nodes. The allowable volume fraction is $v_f = 0.3$. The maximum and minimum member thicknesses are set to $h_{max} = 0.1458$ and $h_{min} = 0.019$ respectively. The required resolution of the continuum domain is 320×160 and the filter radius spans 3 elements. The shape adjacency constraints are set to $b_{l,min} = 0.1$ and $b_{l,max} = 1$ with respect to one cell side size of the ground structure. The penalization function sharpness parameter is set to $\beta_s = 64$ and a penalty continuation is applied. The length ratio of the internal segments of the condensed beam is set to $r_L = 1/3$. The 'patching' stage is skipped during the projection process, to preserve the minimal sizing of flexible hinges.

The results are presented in Table 2. For all cases, the optimization is performed on the lower symmetric half of the domain with symmetry boundary conditions on the top side. Accordingly, the quantitative results correspond to half of the domain but the figures illustrate the full structure.

Table 1: Minimum compliance of an MBB-beam. Beam-based optimization compared to continuum-based robust topology optimization. The beam-based compliance objective is designated f. Its corresponding continuum projection compliance is designated f_{proj}, and the projected volume fraction is $v_{f,proj}$. The continuum optimization compliance objective and volume fraction constraint are designated with the subscript 'cont'.

Volume fraction $v_f = 0.3$	Volume fraction $v_f = 0.5$
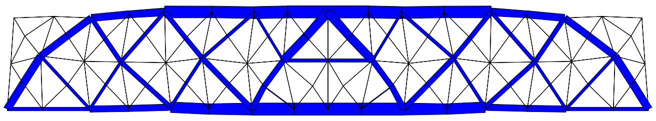	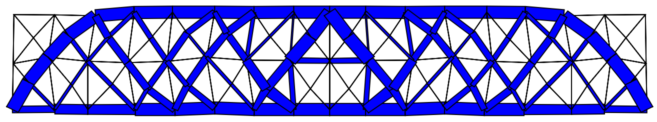
Resulting layouts with tapered beam modeling, full ground structure is superimposed	
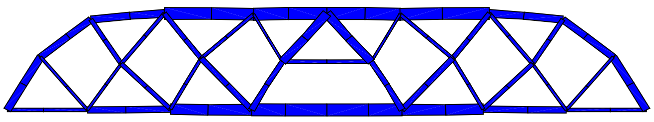	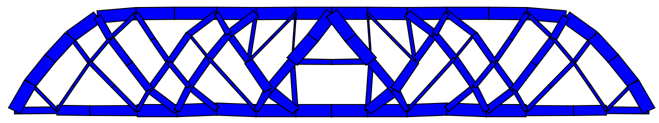
$f = 255.0$, Iter. $= 145$, Time: $= 41s$	$f = 179.3$, Iter.: $= 147$, Time: $= 37s$
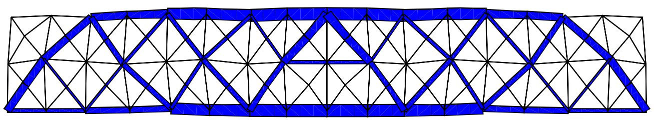	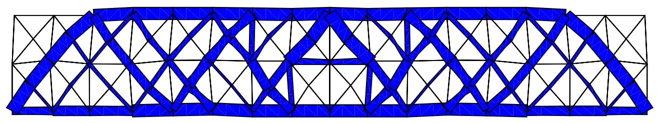
Resulting layouts with condensed beam modeling, full ground structure is superimposed	
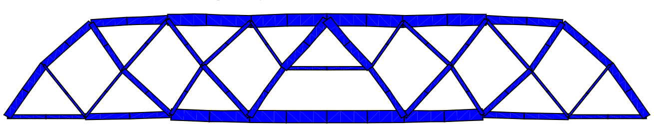	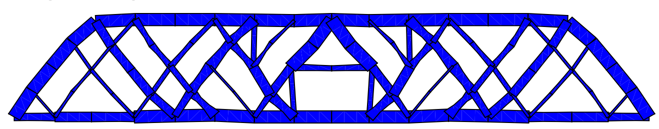
$f = 257.9$, Iter. $= 156$, Time $= 50s$	$f = 188.6$, Iter. $= 201$, Time $= 67s$
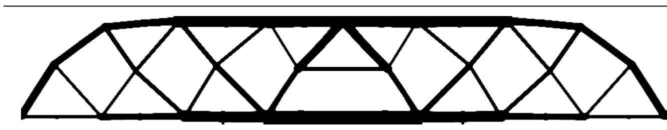	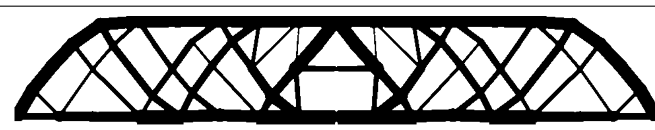
Continuum projection - tapered beam	
$f_{proj} = 317.7$, $v_{f,proj} = 0.26$	$f_{proj} = 237.6$, $v_{f,proj} = 0.41$
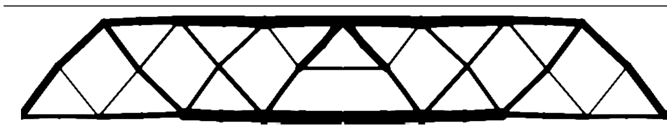	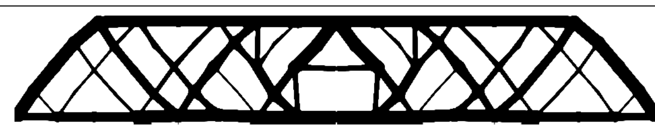
Continuum projection - condensed beam	
$f_{proj} = 322.1$, $v_{f,proj} = 0.26$	$f_{proj} = 236.5$, $v_{f,proj} = 0.41$
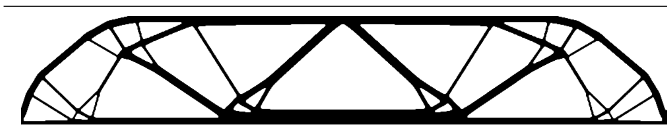	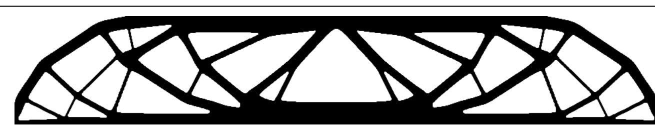
Continuum topology optimization	
$f_{cont} = 324.3$, $v_{f,cont} = 0.26$, Iter. $= 250$, Time $= 322s$	$f_{cont} = 217.4$, $v_{f,cont} = 0.41$, Iter. $= 250$, Time $= 323s$

While both beam-based formulations obtained similar displacement values, the condensed beam formulation provides more consistent design which better resembles conventional continuum designs. This can be attributed to the enhanced design freedom provided by the condensed beam. The negative displacements obtained for both beam formulations are apparently high. However, this positive result is somewhat compromised in the projection to continuum. The main reason is that the flexible hinges cannot be reconstructed well enough in the projection stage due to the flattening of overlapping members. Still, the most important observation is once again the computational efficiency of the beam-based approach. The total run times of the beam-based optimization procedures were 13 and 26 seconds, compared to 1874 seconds for the continuum-based optimization.

The superior computational efficiency and the reduced optimized performance can be effectively balanced in the framework of beam-based optimization that is inherited by continuum topology optimization. The idea is to continue with the robust optimization procedure of Wang et al. [2011] after the projection stage. Results with a volume fraction of $v_f = 0.26$ are presented in Table 3. The optimization ran for 60 iterations with six steps for the continuation of the Heaviside projection. Clearly, the flexible hinges are reconstructed quickly in a few iterations. Hence, this framework gains the advantages of both approaches: the computational efficiency of the beam-based approach and the design freedom of the continuum approach. The final output displacement is slightly better than with the continuum approach, and the computation time is reduced by roughly 80%.

Table 2: Compliant mechanism design. Beam-based optimization compared to continuum-based robust topology optimization. The beam-based displacement objective is designated f. Its corresponding continuum projection is f_{proj} and the projected volume fraction is $v_{f,proj}$. The continuum optimization objective and volume fraction constraint are designated with the subscript 'cont'.

	Beam modeling		Continuum projection
	Regular tapered beam		
$f = -2.60$ $f_{proj} = -1.34$ $v_{f,proj} = 0.26$ Iter. $= 121$ Time $= 13s$	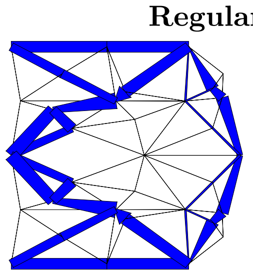 Full ground structure	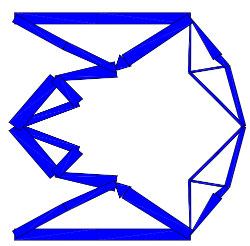	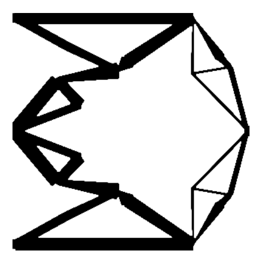
	Condensed beam		
$f = -2.70$ $f_{proj} = -1.31$ $v_{f,proj} = 0.26$ Iter. $= 181$ Time $= 26s$	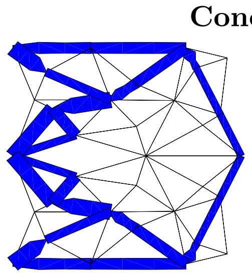 Full ground structure	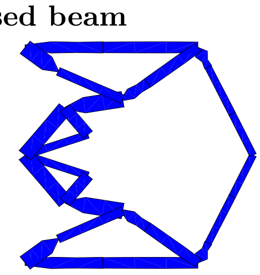	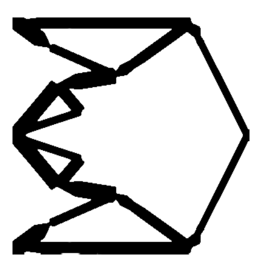
	Robust topology optimization - intermediate design		
	$f_{cont} = -2.20$ $v_{f,cont} = 0.26$ Iter. $= 300$ Time $= 1874s$	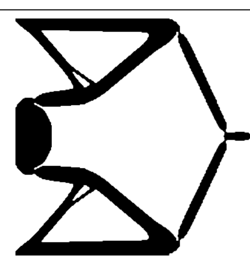	

Table 3: Compliant mechanism design. Results of beam-based optimization inherited by continuum optimization. The continuum projection shown in Table 2 serves as the starting point for the continuum robust topology optimization. The displacement objective is designated f_{inher}.

Regular tapered beam inherited design		**Condensed beam inherited design**	
$f_{inher} = -2.26$ Time $= 392s$	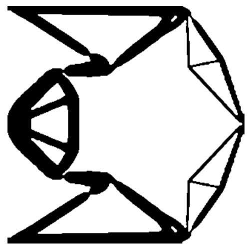	$f_{inher} = -2.27$ Time $= 359s$	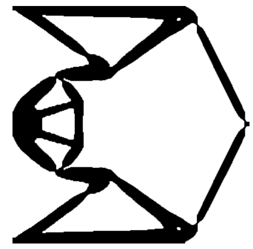

5.3 Minimum compliance of a cantilever beam with maximum length scale

Another set of problems for which the beam-based approach can be beneficial is the design with a maximum length scale, for cases where it is essential for improving the structural redundancy, while compromising the nominal objective value.

In the case of minimum length scale, the continuum approach suggests some well established solutions such as projection techniques [Guest et al., 2004] and the robust topology optimization method [Wang et al., 2011, Sigmund, 2009]. The imposition of maximum length scale in continuum topology optimization is more tricky and was treated by [Guest, 2009], and more recently in [Wu et al., 2016a], [Lazarov et al., 2016] and [Lazarov and Wang, 2017] and still is the concern of ongoing research. Yet, all the solutions of the continuum approach handle this issue by implicitly determining the characteristic sizing. Sometimes such measures also require additional computational effort.

In contrast to the continuum approach, the imposition of length scale by the beam-based approach is explicit and nearly straightforward. The minimum and maximum length scales are dictated by the predefined setting of minimum and maximum thicknesses of the beam members. We demonstrate the maximum length scale imposition utilizing the minimum compliance problem of a cantilever subjected to concentrated load at the middle of its free edge. The results for two volume fractions $v_f = 0.3,\ 0.5$ are shown in Table 4.

The problem is set on a 2×1 domain, discretized by an enriched ground structure with 8×5 nodes. The shape adjacency constraints are $b_{l,min} = 0.15$ and $b_{l,max} = 2$ with respect to one cell side size of the ground structure. The penalty function sharpness parameter is set to $\beta_s = 64$ and a penalty continuation is applied. The minimum thickness is set to $h_{min} = 0.0119$, dictating the FE resolution of the continuum domain to be 320×160. All the examples are solved using the simpler tapered beam formulation. Looking at the computational times, it is clear that the beam-based approach offers an economical and effective means of generating topological layouts with explicit control over the maximum length scale. A fair comparison between the two approaches is a tough task because maximum length scale is implicitly imposed in the continuum approach. For a qualitative comparison of the obtained layouts demonstrated in Table 4, one can examine the results in [Wu et al., 2016a].

5.4 High resolution design

The computational efficiency of the beam-based approach makes it attractive for solving high resolution design problems. Unlike the continuum approach, it solves them without any length scale separation and in reasonable time durations. Yet, the beam-based approach loses the design freedom that the continuum approach has. It is limited inherently to beam members of different sizes and shapes. Nonetheless, many high resolution optimized design layouts consist of beam-like members. Thus, as demonstrated in Tables 5 and 6, in such cases this approach offers designs of real porous-like structures, unlike continuum approach designs that contain periodicity. Rather than topological designs, porous-like structures are highly populated with structural entities. For this reason, thin member penalization is not appropriate and was not used in following examples.

Two minimum compliance high resolution problems are examined herein for different volume fractions: 1) Minimum compliance of a fixed cantilever beam subjected to a concentrated load at the far corner; 2) Minimum compliance of a double clamped beam subjected to two load cases: a concentrated vertical load at the center and each load case in the opposite direction and location. The optimization is performed on half of the domain. The setup of both problems is presented in Figure 13. The design obtained by the beam-based approach for the cantilever problem is compared to the design presented in [Alexandersen and Lazarov, 2015]. As for the double clamped beam problem, the comparison is with respect to the design in [Schury, 2013] The high resolution runs are performed on a standard desktop PC, with Intel-i7-6700K @4GHz CPU and 32GB RAM.

Results of the cantilever beam are presented in Table 5. Applying the beam-based optimization approach to such high resolution problems demonstrates impressively the computational efficiency. Moreover, while the multilevel approach of Alexandersen and Lazarov [2015] generates designs with a

Table 4: Minimum compliance of a cantilever beam with explicit maximum length scale. The regular tapered beam is used. The beam-based compliance objective is designated f. Its corresponding continuum projection compliance is designated f_{proj}, and the projected volume fraction is designated $v_{f,proj}$.

	Beam modeling	**Continuum projection**
Volume fraction $v_f = 0.3$		
High maximum length scale: $h_{max} = 0.1329$		
$f = 85.3$ $f_{proj} = 116.4$ $v_{f,proj} = 0.26$ Iter $= 136$ Time $= 47s$	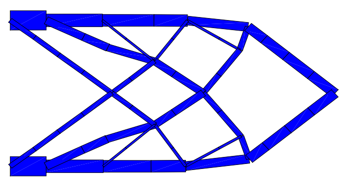	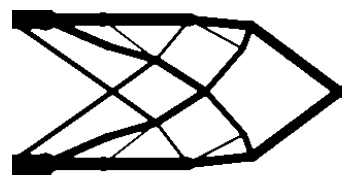
Medium maximum length scale: $h_{max} = 0.0664$		
$f = 93.8$ $f_{proj} = 117.1$ $v_{f,proj} = 0.27$ Iter. $= 147$ Time $= 50s$	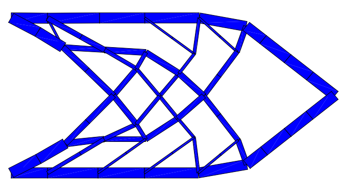	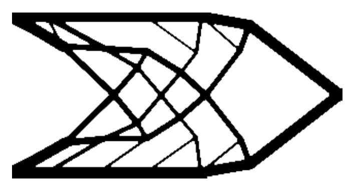
Low maximum length scale: $h_{max} = 0.0418$		
$f = 108.0$ $f_{proj} = 127.9$ $v_{f,proj} = 0.27$ Iter. $= 154$ Time $= 57s$	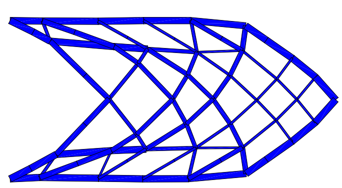	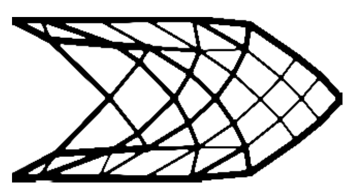
Volume fraction $v_f = 0.5$		
High maximum length scale: $h_{max} = 0.1329$		
$f = 55.8$ $f_{proj} = 77.1$ $v_{f,proj} = 0.41$ Iter. $= 138$ Time $= 41s$	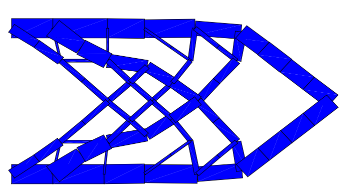	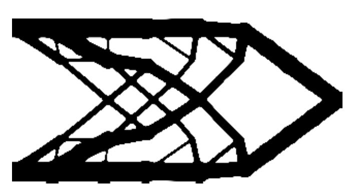
Medium maximum length scale: $h_{max} = 0.0664$		
$f = 67.1$ $f_{proj} = 83.4$ $v_{f,proj} = 0.42$ Iter. $= 158$ Time $= 50s$	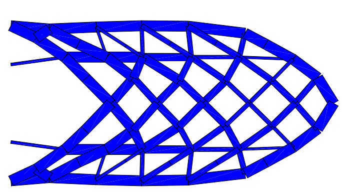	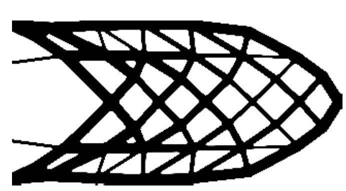
Low maximum length scale: $h_{max} = 0.0418$		
$f = 73.5$ $f_{proj} = 85.7$ $v_{f,proj} = 0.43$ Iter. $= 162$ Time $= 53s$	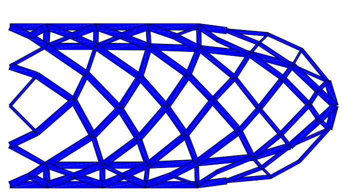	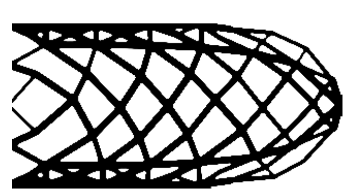

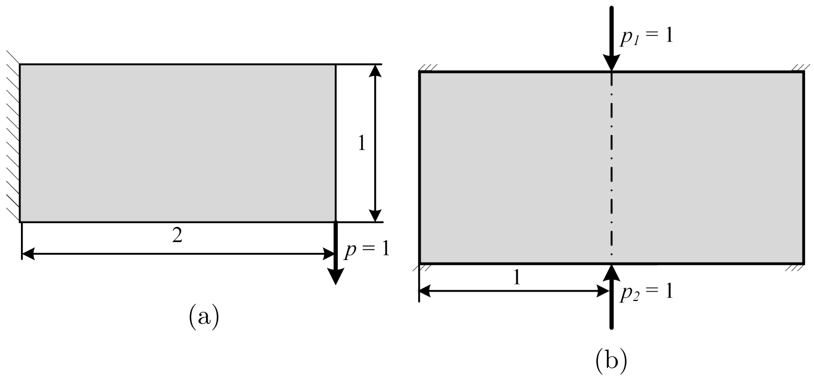

Figure 13: Boundary conditions and loading for the two high resolution problems. (a) Fixed cantilever subjected to a concentrated load at the far low corner; (b) A double clamped beam with two load cases – concentrated vertical loads in opposite directions.

certain imposed periodicity, a non-periodic porous-like structure is obtained by the beam-based approach, which enables the creation of thicker members in the directions of the principal stress trajectories. Thus, it appears that the beam-based optimization is capable of generating fine detailed designs that are complicated to realize by continuum approaches.

Table 5: High resolution design of a fixed cantilever subjected to a concentrated load. The regular tapered beam is used. The compliance objective is designated f.

Volume fraction $v_f = 0.3$			
Grid size	48×24	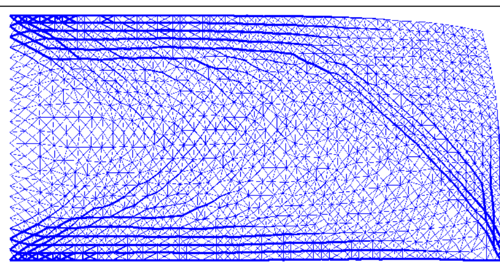	upper left corner 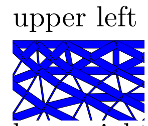 lower right corner 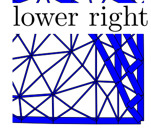
DOFs number	6699		
f	175.4		
Iter.	175		
Time	$8875s$		
Volume fraction $v_f = 0.5$			
Grid size	48×24	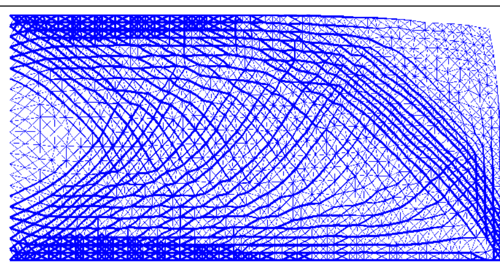	upper left corner 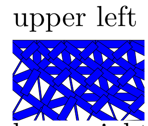 lower right corner 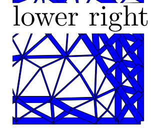
DOFs number	6699		
f	114.1		
Iter.	163		
Time	$10914s$		

The results of the clamped domain are presented in Table 6. In this example, again a porous-like design is obtained. Thick members are directed in the principal stress trajectories, such that the structure can withstand both expected shear and bending loads. This result resembles the design obtained in the hierarchical approach presented by Schury [2013] with reduced computational resources. Moreover, no means of bridging between scales are required. Once again, although the beam-based approach is considered a discrete domain strategy, the material of the optimized design is well distributed, and a detailed one-level layout is obtained.

6 Conclusions

A structural optimization approach based on beam modeling is introduced and investigated. This approach utilizes a two-phase optimization scheme, parametrized on a discrete enriched nodes ground structure with alternating shape and sizing-topology design updates. Two formulations of the beam members are investigated: 1) A linear tapered beam with two thickness variables at its ends; 2) A beam composed of three segments with four controlling thicknesses, formulated by static condensation. A scheme that switches smoothly to an approximated formulation in the vicinity of the prismatic case prevents numerical instability. Throughout the numerical examples section, the significant computational efficiency is exposed consistently by comparison to continuum-based topology optimization. For minimum compliance problems, the consequence is that the beam-based modeling approach offers a computationally cheap alternative that can generate designs that perform similarly to continuum-based designs. For problems that involve the synthesis of flexible hinges such as in compliant mechanism design, though seemingly the method obtains superior results, the performance deteriorates when reconstructing the

Table 6: High resolution design of double clumped beam subjected to two load cases. The regular tapered beam is used. The compliance objective is designated f.

Volume fraction $v_f = 0.3$

Grid size	32×32	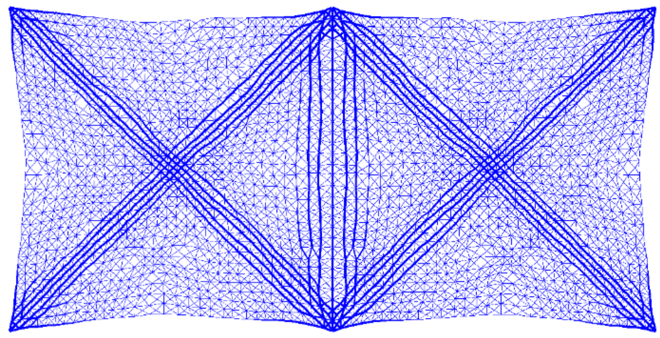	upper left corner 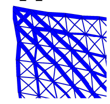
DOFs number	5955		half domain center 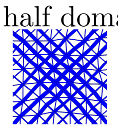
f	36.9		lower middle 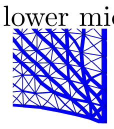
Iter.	141		
Time	$4984s$		

Volume fraction $v_f = 0.5$

Grid size	32×32	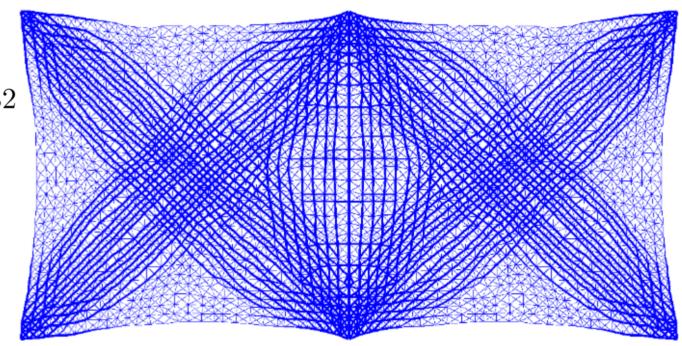	upper left corner 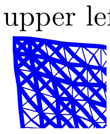
DOFs number	5955		half domain center 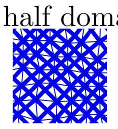
f	23.7		lower middle 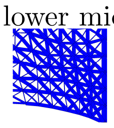
Iter.	123		
Time	$4983s$		

layout on the continuum domain. Therefore it is suggested to use beam modeling optimization as an initial stage for generating an 'educated guess' that serves as a starting point for continuum-based optimization.

The beam-based approach offers an explicit means of imposing consistent length scales, especially maximum length scale which is still a rather open research topic. Thus, by predefining the minimum and maximum thicknesses of the beam members, the design length scale properties are determined in accordance with the functional requirements. The main advantage of the beam-based approach which is the computational efficiency, is further utilized for high resolution problems. Non-uniform and non-periodic porous-like structures can be designed by performing a single-level optimization process. A fine detailed design is obtained unlike any of the designs obtained by utilizing a continuum-based optimization strategy.

The regularity and manufacturability of the optimized layout are kept by constraining nodes positioning and by controlling members sizing. The nodes positioning constraints preserve the structural regularity on the one hand and enable large node movements on the other hand, hence enhancing the design freedom.

Future work will focus on improving the representation and subsequent optimization of flexible hinges, as well as on various possibilities of extending the approach to 3-D. As high resolution 3-D continuum topology optimization is extremely costly in terms of computational effort, alternatives using discrete members can be attractive, especially in the context of AM – as suggested with trusses [Smith et al., 2016]. Thus we believe that the proposed beam-based shape and sizing-topology scheme is well worth exploring.

References

N. Aage, E. Andreassen, and B. S. Lazarov. Topology optimization using petsc: An easy-to-use, fully parallel, open source topology optimization framework. Structural and Multidisciplinary Optimization, 51(3):565–572, 2014.

N. Aage, E. Andreassen, B. S. Lazarov, and O. Sigmund. Giga-voxel computational morphogenesis for structural design. Nature, 550(7674):84, 2017.

W. Achtziger. On simultaneous optimization of truss geometry and topology. Structural and Multidisciplinary Optimization, 33(4-5):285–304, 2007.

J. Alexandersen and B. Lazarov. Topology optimisation of manufacturable microstructural details without length scale separation using a spectral coarse basis preconditioner. Computer Methods in Applied Mechanics and Engineering, 290:156–182, 2015.

E. Andreassen, B. Lazarov, and O. Sigmund. Design of manufacturable 3d extremal elastic microstructure. Mechanics of Materials, 69(1):1–10, 2014.

K.-J. Bathe. Finite element procedures. Klaus-Jurgen Bathe, 2006.

A. Ben-Tal, M. Kočvara, and J. Zowe. Two nonsmooth approaches to simultaneous geometry and topology design of trusses. In Topology Design of Structures, pages 31–42. Springer, 1993.

M. Bendsøe and O. Sigmund. Material interpolation schemes in topology optimization. Archive of applied mechanics, 69(9):635–654, 1999.

M. Bendsøe and O. Sigmund. Topology optimization: theory, methods, and applications. Springer Science & Business Media, 2003.

M. P. Bendsøe and N. Kikuchi. Generating optimal topologies in structural design using a homogenization method. Computer methods in applied mechanics and engineering, 71(2):197–224, 1988.

B. Bourdin. Filters in topology optimization. International Journal for Numerical Methods in Engineering, 50:2143–2158, 2001.

T. E. Bruns and D. A. Tortorelli. Topology optimization of non-linear elastic structures and compliant mechanisms. Computer Methods in Applied Mechanics and Engineering, 190:3443–3459, 2001.

V. Challis, A. Roberts, and J. Grotowski. High resolution topology optimization using graphics processing units (gpus). Structural and Multidisciplinary Optimization, 49(2):315–325, 2014.

P. W. Christensen and A. Klarbring. An Introduction to Structural Optimization. Springer, 2009.

A. Clausen and E. Andreassen. On filter boundary conditions in topology optimization. Structural and Multidisciplinary Optimization, pages 1–9, 2017.

W. Cleghorn and B. Tabarrok. Finite element formulation of a tapered timoshenko beam for free lateral vibration analysis. Journal of sound and vibration, 152(3):461–470, 1992.

J. Deaton and R. Grandhi. A survey of structural and multidisciplinary continuum topology optimization: post 2000. Structural and Multidisciplinary Optimization, 49(1):1–38, 2014. ISSN 1615-147X. doi: 10.1007/s00158-013-0956-z. URL http://dx.doi.org/10.1007/s00158-013-0956-z.

M. Eisenberger. Stiffness matrices for non-prismatic members including transverse shear. Computers & Structures, 40(4):831–835, 1991.

S. Gavranovic, D. Hartmann, and U. Wever. Topology optimization using gpgpu. Master's thesis, Masters thesis, Technical University Munich, 2015.

L. Gil and A. Andreu. Shape and cross-section optimisation of a truss structure. Computers & Structures, 79(7):681–689, 2001.

J. Groen and O. Sigmund. Homogenization based topology optimization for high resolution manufacturable micro structures. International Journal for Numerical Methods in Engineering, 2017.

J. Guest. Imposing maximum length scale in topology optimization. Structural and Multidisciplinary Optimization, 37(5):463–473, 2009.

J. Guest, J. Prévost, and T. Belytschko. Achieving minimum length scale in topology optimization using nodal design variables and projection functions. International journal for numerical methods in engineering, 61(2):238–254, 2004.

B. Lazarov and F. Wang. Maximum length scale in density based topology optimization. Computer Methods in Applied Mechanics and Engineering, 2017.

B. Lazarov, F. Wang, and O. Sigmund. Length scale and manufacturability in density-based topology optimization. Archive of Applied Mechanics, 86(1-2):189–218, 2016.

MATLAB. MATLAB version 8.1.0.604 (R2013a). The MathWorks, Natick, Massachusetts, 2013.

A. Ramos Jr and G. Paulino. Filtering structures out of ground structures–a discrete filtering tool for structural design optimization. Structural and Multidisciplinary Optimization, 54(1):95–116, 2016.

S. Schmidt and V. Schulz. A 2589 line topology optimization code written for the graphics card. Computing and Visualization in Science, 14(6):249–256, 2011.

F. Schury. Two Scale Material Design From Theory to Practice. PhD thesis, University of Erlangen Nuremberg, Erlangen Nuremberg, 6 2013.

F. Schury, M. Stingl, and F. Wein. Efficient two scale optimization of manufacturable graded structures. SIAM Journal on Scientific Computing, 34(6):B711–B733, 2012.

O. Sigmund. Materials with prescribed constitutive parameters: an inverse homogenization problem. International Journal of Solids and Structures, 31(17):2313–2329, 1994.

O. Sigmund. A new class of extremal composites. Journal of the Mechanics and Physics of Solids, 48(2): 397–428, 2000.

O. Sigmund. Manufacturing tolerant topology optimization. Acta Mechanica Sinica, 25(2):227–239, 2009.

O. Sigmund and K. Maute. Topology optimization approaches. Structural and Multidisciplinary Optimization, 48(6):1031–1055, 2013.

C. J. Smith, M. Gilbert, I. Todd, and F. Derguti. Application of layout optimization to the design of additively manufactured metallic components. Structural and Multidisciplinary Optimization, 54(5): 1297–1313, 2016.

K. Suresh. Efficient generation of large-scale pareto-optimal topologies. Structural and Multidisciplinary Optimization, 47(1):49–61, 2013.

K. Svanberg. The method of moving asymptotesa new method for structural optimization. International journal for numerical methods in engineering, 24(2):359–373, 1987.

E. Wadbro and M. Berggren. Megapixel topology optimization on a graphics processing unit. SIAM review, 51(4):707–721, 2009.

F. Wang, B. Lazarov, and O. Sigmund. On projection methods, convergence and robust formulations in topology optimization. Structural and Multidisciplinary Optimization, 43(6):767–784, 2011.

W. Weaver and J. Gere. Matrix Analysis Framed Structures. Springer Science & Business Media, 2012.

J. Wu, N. Aage, R. Westermann, and O. Sigmund. Infill optimization for additive manufacturing - approaching bone-like porous structures. arXiv preprint arXiv:1608.04366, 2016a.

J. Wu, C. Dick, and R. Westermann. A system for high-resolution topology optimization. IEEE transactions on visualization and computer graphics, 22(3):1195–1208, 2016b.

T. Zegard and G. H. Paulino. Toward GPU accelerated topology optimization on unstructured meshes. Structural and Multidisciplinary Optimization, 48(3):473–485, 2013. doi: 10.1007/s00158-013-0920-y.